
Sub-micron spatial resolution in far-field Raman imaging via positivity constrained super-resolution

Journal Title
XX(X):2-19
c The Author(s) 2018 Reprints and permission:
sagepub.co.uk/journalsPermissions.nav
DOI: 10.1177/ToBeAssigned
www.sagepub.com/



Dominik J. Winterauer^{1,2}, Daniel Funes-Hernando², Jean-Luc Duvail², Saïd Moussaoui³, Tim Batten¹ and Bernard Humbert²

Abstract

Raman microscopy is a valuable tool for detecting physical and chemical properties of a sample material. When probing nanomaterials or nanocomposites the spatial resolution of Raman microscopy is not always adequate as it is limited by the optical diffraction limit. Numerical post-processing with super-resolution algorithms provides a means to enhance resolution and can be straightforwardly applied. The aim of this work is to present interior-point least squares (IPLS) as a powerful tool for super-resolution in Raman imaging through constrained optimisation. IPLS's potential for super-resolution is illustrated on numerically generated test images. Its resolving power is demonstrated on Raman spectroscopic data of a polymer nanowire sample. Comparison to AFM data of the same sample substantiates that the presented method is a promising technique for analysing nanomaterial samples.

¹Renishaw plc

²Institut des Matériaux Jean Rouxel Nantes (IMN)

³Laboratoire des Sciences du Numérique de Nantes

Corresponding author:

Dominik J. Winterauer, Renishaw plc, New Mills, Wotton-under-Edge, Gloucestershire, GL12 8JR, United Kingdom. Tel: +44 1453 524524

Email: dominik.winterauer@protonmail.com

Keywords

Super-resolution; Digital image restoration; Raman spectroscopy; Nanomaterials

Introduction

Super-resolution image reconstruction (SRIR) uses signal processing techniques to overcome the resolution limitation of conventional (optical) imaging apparatus¹, usually by combining multiple images of the same scene². A multitude of numeric SRIR methods based on different philosophies are available in the literature¹ and various super-resolution algorithms have been employed for SRIR in Raman spectroscopy mapping over the last decade³⁻⁶. The application of SRIR to Raman spectroscopy is a promising method that allows distances and objects below the diffraction limit to be resolved using far-field instrumentation, without the added experimental complexity of near-field techniques such as nearfield Raman spectroscopy (NFRS)^{7,8} or tip-enhanced Raman spectroscopy (TERS)^{9,10}. While the concept of SRIR is already very powerful in itself, it still takes adequate optimisation algorithms to unleash its full potential.

A promising approach to SRIR is constrained optimisation, which has been successfully applied in image inpainting¹¹, non-negative matrix factorisation^{12,13}, and achieved great resolution enhancements in digital image restoration, whether the constraint was used explicitly¹⁴, or implicitly by the choice of regularisation function¹⁵⁻¹⁷.

In this work a primal-dual method for interior-point least squares (IPLS)¹⁸ was used for constrained optimisation SRIR. IPLS was applied to Raman spectroscopic data acquired from a bundle of nanowires made of poly-(3,4 ethylenedioxythiophene) here referred to as PEDOT^{19,20}. Atomic force microscopy (AFM) images were obtained from the same sample area. AFM imaging is not affected by the optical diffraction limit and hence provides a means to evaluate the quality of the super-resolved Raman images.

The discussion of the results focuses on the resolving power of SRIR, a point that was sometimes ambiguous in related work. The ambiguity arises from the two research disciplines overlapping in Raman SRIR,

digital image restoration and microscopy, having slightly different notions of *resolution*. In digital image restoration resolution is usually seen as the level of detail contained in an image and often characterised by the sharpness of features in the image, a point of view that has been adopted in previous work on SRIR in Raman imaging³⁻⁶. Resolution in microscopy, on the other hand, is defined by the minimal separation between two objects necessary to observe them as distinct objects. SRIR results in Raman imaging have not been analysed from that perspective and while the two points of view are somewhat related they are not strictly identical.

The aim of this paper is to highlight the difference between these two interpretations of resolution and to demonstrate that Raman SRIR is capable of resolving distances smaller than the diffraction limit in the strict microscopist's sense.

Materials and methods

Sample preparation

PEDOT nanowires were synthesised by the hard template method described in a previous paper²⁰. The template was an anodic aluminium oxide membrane of $(50 \pm 1)\mu\text{m}$ thickness and $(100 \pm 10)\text{nm}$ pore diameter (Synkera Unikera SM 100-50-13). The pore diameter constrains the diameter of the synthesised nanowires. The sonicated PEDOT nanowires were dispersed in water and drop cast on a silicon substrate²⁰. The dispersion, as most dispersions of nano-objects in water, is incomplete and the nanowires tend to stick in bundles of different sizes, shapes and numbers of nanowires, although some of them were found isolated (see fig. 3a).

Instrumentation

Raman spectroscopic measurements were performed using a confocal Raman microscope (Renishaw inVia) with a 532nm frequency doubled Nd-YAG laser as the excitation source. A 100×0.85 NA objective lens was used to focus the laser onto the sample and to collect the Raman back scattered light. The laser was linearly polarised along the vertical image axis. Laser power on the PEDOT sample was 0.1mW with acquisition time 0.5s per spectrum. With these parameters no bleaching or other photo

induced modification of the sample was observed. The system was operated in high confocal mode to ensure the best lateral resolution was achieved. Raman mapping was conducted under the microscope using a motorised piezo-electric stage (Physikinstrumente Hera P621.2CD XY) in closed loop operation (0.4nm resolution, 2nm repeatability). Data were collected by point mapping in a raster scanning fashion and each Raman spectrum is acquired under identical conditions. For this work a 20nm step size was used.

The Raman system with the piezo stage rests on an optical table that is passively damped and any environmental vibrations were not seen to be a significant issue. Measurement parameters were optimised to reduce measurement times to avoid artefacts originating from other environmental factors such as thermal drift.

Atomic force microscopy (AFM)²¹ was performed with a scanning probe microscope (Bruker Innova) operated in tapping mode²². The AFM tips used were Olympus AC160TS-10 (OTESPA) AFM tips in visible apex geometry with a side and back angle of $35^\circ \pm 1^\circ$ each, a front angle of $0^\circ \pm 1^\circ$, and a maximum tip radius of 10nm²³. AFM imaging is a high-resolution imaging technique and served as validation of the results obtained by SRIR from the Raman data. For samples with high aspect ratios, and heights exceeding the tip curvature radius, the lateral resolution

of the AFM is adversely affected by the tip geometry^{24–26}. Since the diameters of the studied PEDOT nanowires were well in excess of the tip radius, tip geometry effects were visible in the AFM images obtained. Tip geometry effects, however, only broaden the apparent width of objects, while position, height, orientation, and alignment are imaged faithfully and the obtained lateral resolution was still significantly better than that of the diffraction limited Raman microscope.

Super-resolution image restoration

SRIR relies on inverse problem resolution and thus needs three ingredients to work properly: an observation model, an optimisation criterion, and a powerful optimisation algorithm²⁷.

The observation model describes how an ideal high-resolution image transforms into a blurry and noisy image through the distortions imposed

by the imaging apparatus and the imaging process. Observation models in digital optical imaging can be written in the compact linear form^{1,28,29}

$$y = Hx + \eta. \tag{1}$$

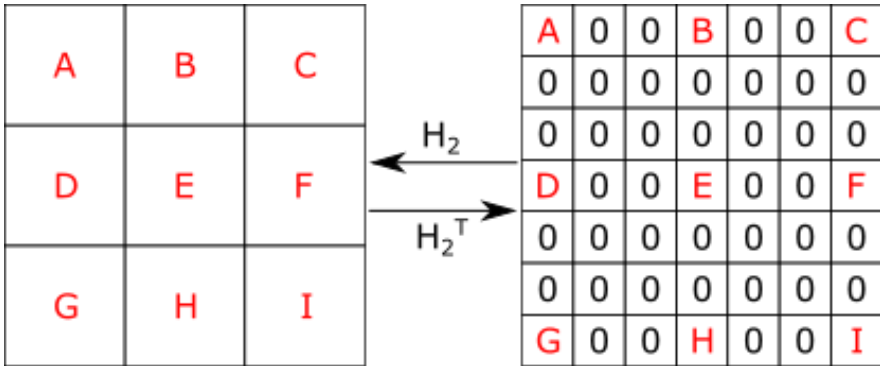


Figure 1. Illustration of the up- and downsampling process: The alphabetically labelled pixels in the low-resolution image (left) are identical to the alphabetically labelled pixels in the high-resolution image (right). The ‘0’-labelled pixels in the high-resolution image have no correspondence in the low-resolution image, these are the pixels that have been (artificially) inserted. They are equal to 0 when H^T_2 is applied to the low-resolution image.

Each index of column vector y corresponds to one of the M pixels in the low-resolution image. Likewise, each index of the column vector x corresponds to one of the N pixels in the high-resolution picture. The $M \times N$ matrix H is the *forward operator* which describes the weights with which each pixel intensity in the high-resolution picture x affects each pixel intensity in the low-resolution image y . The additive term η accounts for any non-deterministic process during imaging and is usually modelled as independent and identically distributed (i.i.d.) Gaussian noise. For the present case the linear degradation H is factored into two terms¹

$$H = H_2H_1. \tag{2}$$

H_1 corresponds to a 2D convolution with the microscope's *point-spread function* (PSF) and H_2 represents downsampling. The former is ubiquitous in microscopy and gives rise to the well-known diffraction limit in conventional optical microscopes. The PSF depends on the specifications of the instrument and will be determined experimentally below.

If the high-resolution image x has more pixels than the observed low-resolution image y a decimation or downsampling operation H_2 has to

be included in the observation model^{1,29,30}. Conversely, its transpose H_2^T is known as upsampling and describes the manner in which pixels are added to the low-resolution image. The upsampling operation H_2^T is dependent on the pixel dimensions of the high-resolution image which in most cases can be chosen as desired. The corresponding downsampling operation H_2 is found by transposition. Additional pixels can be added with equal spacing along each dimension between existing pixels in the low resolution image y . The point mapping nature of the confocal imaging process means that there is a one to one correspondence between the low-resolution image pixels and a subset of the pixels in the high-resolution image. Fig. 1 shows the case where two high-resolution pixels are inserted between each two low-resolution pixels along each dimension.

SRIR in this paper is performed by interior-point least squares (IPLS). The optimisation criterion solved is

$$\hat{x} = \underset{x}{\operatorname{argmin}} (y - Hx)^T (y - Hx) \quad (3a)$$

$$\text{s.t. } \mathbf{x} \succeq 0, \quad (3b)$$

The positivity constraint on the pixel intensities, eq. (3b), reflects the natural assumption that abundances of scattering sources can only be nonnegative. Given y and H are known, eq. (3) can be solved by a primaldual optimisation method for IPLS¹⁸. SRIR via eq. (3) on numerically generated test data with known degradation H is demonstrated in the supplemental material.

PSF measurement

The instrument's PSF enters the forward operator H through H_1 , eq. (2). Because H must be known for solving eq. (3), the PSF of the instrument has to be determined prior to any SRIR. The Raman microscope used in this work probes the sample with an excitation laser. It can be reasoned from the beam shape of lasers in resonators, the subsequent optics^{31–34}, and the response function of optical microscopes³⁵ that the intensity profile of the PSF is approximately Gaussian.

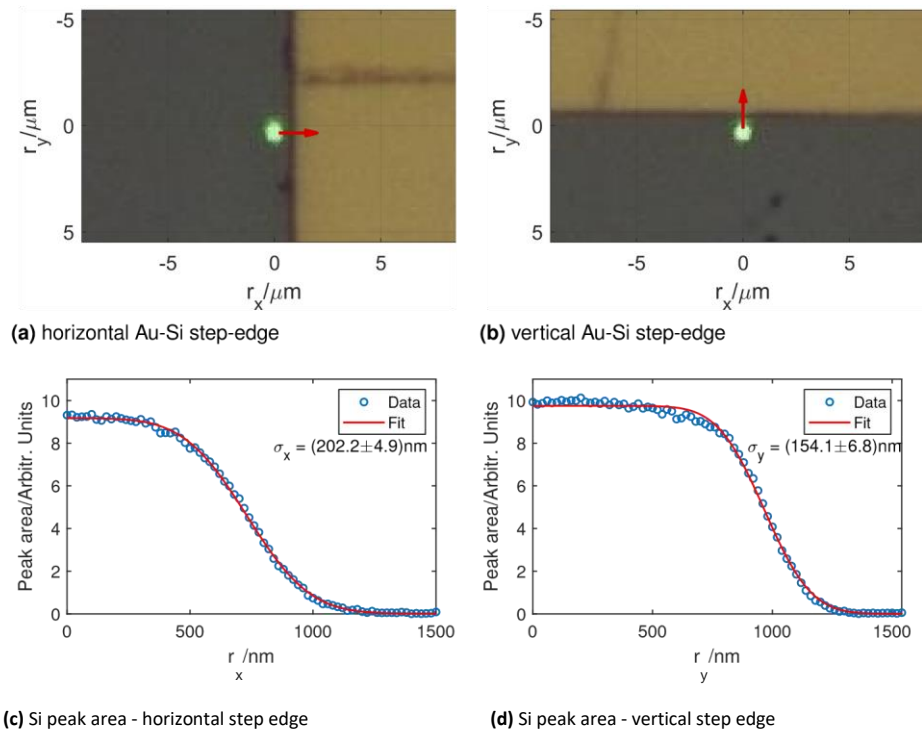


Figure 2. Measurement of the microscope PSF: Optical images of the horizontal (a) and vertical (b) Au-Si step-edge. The Raman signal is acquired along the red arrows with a sampling step of 20 nm. The area of the principle Si peak at 520.7cm^{-1} is calculated for each sampling point and plotted against the distance (c, d). The model function eq. (5) is fitted to the data.

A general 2D Gaussian takes 3 independent parameters but from the symmetry of the instrument's configuration it can be assumed that its

functional dependency factorises along the stage axes. Thus, the PSF is sufficiently described by

$$p(r_x, r_y) \propto \exp\left(-\left(\frac{r_x^2}{2\sigma_x^2} + \frac{r_y^2}{2\sigma_y^2}\right)\right), \quad (4)$$

where r_x and r_y are the coordinates along the stage axes. This is supported by the data shown in fig. 2. The parameters σ_x and σ_y in eq. (4) were determined experimentally using the step-edge criterion.

The laser was scanned over the edge of a gold pad deposited on a silicon substrate. (figs. 2a and 2b). Raman scattering only occurs when laser light falls on the silicon and not on the metallised region. The resulting intensity profile is a 1D line integral of eq. (4) that can be modelled by

$$\phi(r, a, b, \mu, \sigma) = a + \frac{b}{2} \left(1 + \operatorname{erf}\left(\frac{r - \mu}{\sqrt{2}\sigma}\right)\right). \quad (5)$$

For horizontal and vertical step edges σ in eq. (5) is equal to σ_x and σ_y in eq. (4), respectively. Fig. 2 shows the peak area profile of the principal silicon Raman peak across a horizontal and vertical step-edge. The peak area was calculated by integrating the Raman signal from 480cm^{-1} to 562cm^{-1} in the wavenumber domain, which contains the principal Raman peak of silicon (found at 520.7cm^{-1}). Prior to integration a linear background was subtracted from each spectrum to remove any interfering fluorescence signal. Eq. 5 is fit to each of the profiles and the values obtained for σ are

$$\sigma_x = (202.2 \pm 4.9) \text{ nm} \quad (6a) \quad \sigma_y = (154.1 \pm 6.7)$$

$$\text{nm}. \quad (6b)$$

These correspond to full widths at half maximum (FWHM) of

$$FWHM_x = (476.1 \pm 11.5) \text{ nm} \quad (7a)$$

$$FWHM_y = (362.9 \pm 15.8) \text{ nm}, \quad (7b)$$

which can be used as a measure for the minimum resolvable distance of the instrument in the respective direction (see supplemental material for more details). The Raman data for PSF measurement were acquired with $20mW$ laser power at $532nm$, $0.2s$ acquisition time per spectrum and $20nm$ step size.

Results

Raman and AFM mapping of PEDOT nanowires

An optical image of the PEDOT nanowire sample area is shown in fig. 3a. A map of $1.2\mu m \times 1.5\mu m$ is collected from within the red rectangle displayed. The Raman data of PEDOT nanowires are acquired with $0.1mW$ laser power at $532nm$, $0.5s$ acquisition time per spectrum and a step size of $20nm$ along each stage axis. Fig. 3b shows a PEDOT Raman spectrum. The two main peaks at $1437cm^{-1}$ and $1518cm^{-1}$ are attributed to the symmetric and anti-symmetric vibration modes of the aromatic C=C bond, respectively¹⁹.

The Raman intensity of the spectral channel centred at the peak position of the dominant C=C peak ($1437cm^{-1}$) is plotted as a heat map over the

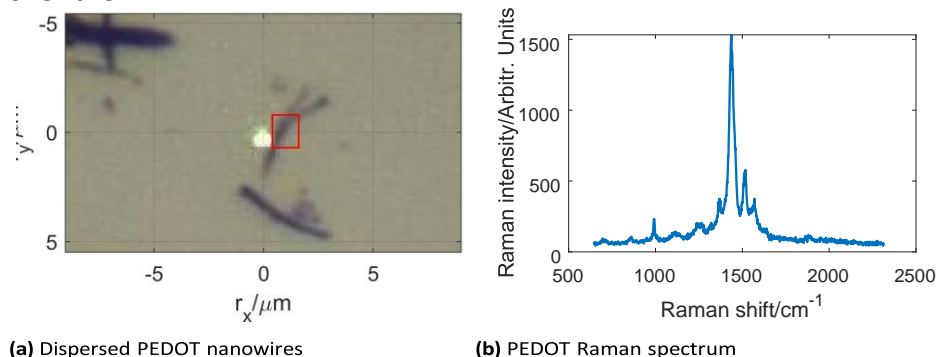


Figure 3. The PEDOT sample: (a) Optical image of PEDOT nanowires dispersed on a Si substrate: The Raman data is collected from within the red rectangle of $1.2\mu m \times 1.5\mu m$. The bright green dot at the origin is a visualisation of the $532nm$ laser spot. (b) PEDOT Raman spectrum: The dominant peak at $1437cm^{-1}$ is caused by the symmetric vibration mode of the aromatic C=C bond¹⁹.

sampling area in fig. 4a. An AFM map of size $3\mu\text{m} \times 3\mu\text{m}$ covering the area probed by Raman spectroscopy was acquired for comparison. The number of sampling points was 512×512 , resulting in a pixel size of approximately $6\text{nm} \times 6\text{nm}$. The measured height across the Raman probed area is shown in fig. 4b. Two nanowires separating from each other at the top of the mapping area, as visualised in fig. 4b, cause the spatial broadening of the Raman signal perpendicular to the direction of the wire observed in fig. 4a. However, the separation of the two wires within the sampling areas is smaller than any of the minimum resolvable distances of the Raman microscope, eq. (7), and hence they cannot be directly observed as individual wires.

Image restoration results

With knowledge of the PSF parameters eq. (6) H_1 in eq. (2) is fully specified and eq. (3) can be solved for the Raman map data of fig. 4a for different choices of H_2 . The first choice was identity, resulting in a pixel size of $20\text{nm} \times 20\text{nm}$ (' 20nm ' for brevity, fig. 5a), identical to that in the observed image fig. 4a. The second choice was such that the resulting pixel size was $10\text{nm} \times 10\text{nm}$ (' 10nm ' for brevity, fig. 5b).

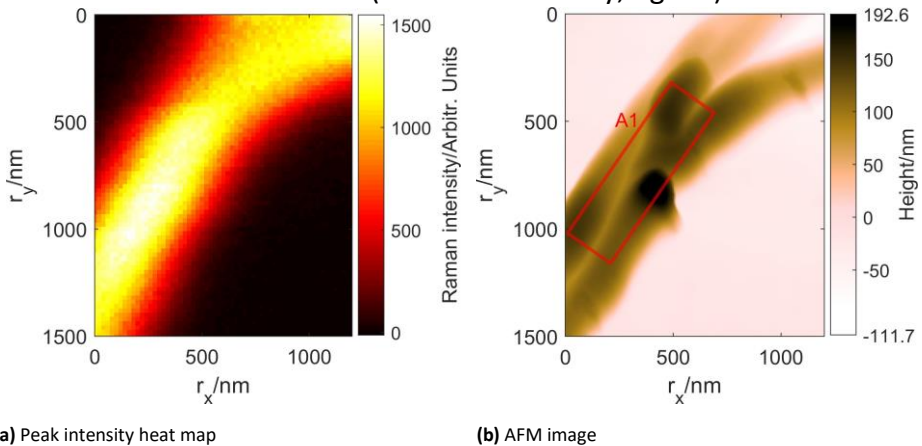


Figure 4. (a) The Raman intensity of the spectral channel centred at the peak position of the dominant C=C peak (1437cm^{-1}) plotted as a heat map over the sampling area. Pixel size is $20\text{nm} \times 20\text{nm}$ (b) An image of the sampling area obtained by atomic force microscopy. 2-3 PEDOT nanowires can be distinguished within the bundle. The red area 'A1' is marked for comparison with the SRIR images shown in fig. 5. The apparent width of the wires is

broadened relative to their true width due to tip geometry effects^{24,26}. Height, position, orientation, and alignment are imaged faithfully. Pixel size is $6\text{nm} \times 6\text{nm}$.

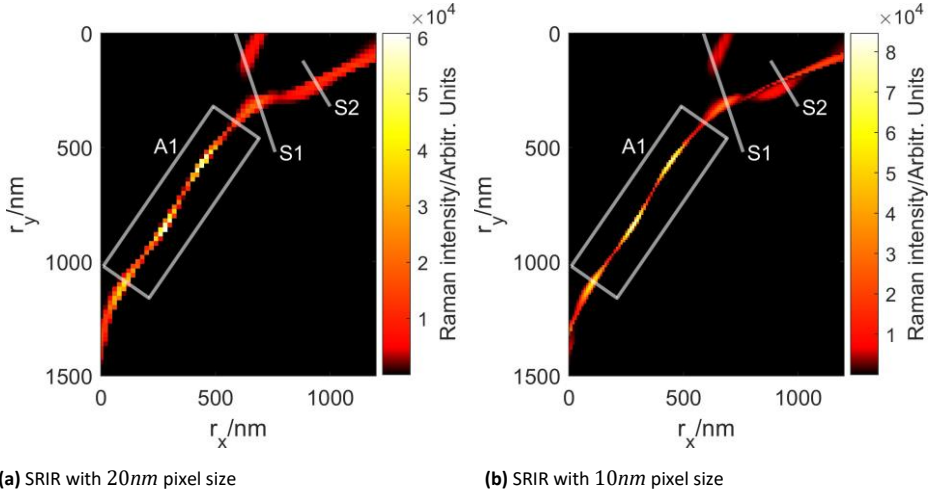


Figure 5. Super-resolution of the Raman heat map shown in fig. 4a for a resulting pixel sizes of (a) 20nm and (b) 10nm . Two separate wires can be resolved at the top of each image. Line profiles along the sections S1 and S2 for both figures are shown in fig. 6.

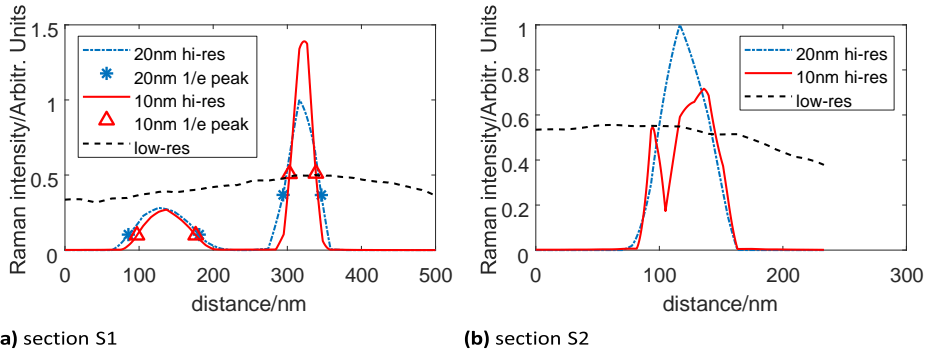


Figure 6. Line profiles along image sections of fig. 5: (a) Line intensity profile along section S1: Two objects are resolved, each of them appearing as a peak. The two peak maxima are separated by 189.8nm (20nm) and 186.0nm (10nm). The edges of the objects are located at the points where the intensity drops to $1/e$ times the peak intensity and are marked by stars (20nm) and triangles (10nm). The distance between the edges of the two objects are 113.2nm and 126.6nm , respectively. (b) Line intensity profile along section S2: A single peak in the 20nm pixel size SRIR image can be resolved as two peaks in the 10nm pixel size SRIR image. The black dashed lines are the corresponding line profiles in the low-resolution image fig. 4a. The line profiles are obtained through linear interpolation of the respective images.

The properties of the SRIR results can be examined along the sections S1 and S2 shown in fig. 5. The corresponding line profiles obtained by linear interpolation are shown in fig. 6.

The super-resolved Raman images in fig. 5 do not match perfectly with the AFM image in fig. 4b but they illustrate the position, alignment, and orientation of the nanowires in good agreement with this image. They are much sharper and show more features than the observed low-resolution Raman image fig. 4a.

Discussion

Sharpness and Resolution

Downsampling in the forward operator of single-frame super-resolution renders the unconstrained optimisation problem eq. (3a) ill-posed. In multi-frame super-resolution this is compensated by the acquisition of multiple low-resolution images resulting in a total number of observed pixels that is equal to or larger than the number of pixels in the superresolved image, thus reinstating well-posedness. In the present work lost high spatial frequency information was recovered by the positivity constraint eq. (3b) and its implementation through primal-dual IPLS. This allowed for the reconstruction of the sharp high-resolution image fig. 5b with 10nm pixel size from just a single observation fig. 4a with 20nm pixel size. Comparison of fig. 5a and fig. 5b, as well as the line profiles of fig. 6, show that the super-resolved image with 10nm pixel size is much sharper than that with 20nm pixel size. While this is a very exciting result from an image restoration point of view, detailed analysis reveals the gain in sharpness does not necessarily corresponds to a gain in resolution.

The edges in the line profiles shown in figs. 6a and 6b have widths well below 50nm for both high-resolution images shown in fig. 5. However, this does not mean that the obtained resolvable distance is 50nm or smaller in each case. This is illustrated along the area A1 in fig. 5 where the SRIR results only show one nanowire with high intensity, while the corresponding AFM image in fig. 4b clearly shows 2-3 wires in the same area. The SRIR results show two separate nanowires only in areas where

the two wires are separated further than the SRIR minimum resolvable distance, which can be estimated from the line profiles along the section S1 in fig. 6a. The two peaks observed correspond to two different nanowires that can be distinguished as two different objects. The peak to peak distance between their maximum intensities is 189.8nm and 186.0nm for 20nm and 10nm pixel size, respectively. For point-like objects this would give a measure of the spatial resolution. However, as known from the fabrication process and confirmed by AFM in fig. 4b we are dealing with objects of finite size and a more suitable measure would be their edge separation. Since their edges are not sharp, the edge positions were chosen to be at $1/e \approx 0.368$ times the peak intensities. The resulting edge separations are 113.2nm and 126.6nm for 20nm and 10nm pixel size, respectively, which is much larger than the observed width of edges for both cases. Although the width of edges and other features, which determines the sharpness of an image, puts a lower bound on the minimum resolvable distance, a measure for resolution, sharpness and resolution are two distinct properties and thus should be treated as such. Further, the apparent increase in sharpness in the 10nm pixel size super-resolved image compared to the 20nm pixel size one is not reflected in the achieved minimum resolvable distance.

This, however, should not obscure the satisfying result that the larger minimum resolvable distance, 126.6nm , is about a factor 3 smaller than $FWHM_y = 362.9\text{nm}$, the smallest value obtained for the instrument's minimum resolvable distance.

Comparison to AFM image

Despite the enhanced resolution SRIR images still mismatch with the AFM image for a number of reasons. The minimum resolvable distance in AFM is well below 10nm (for objects of similar height), i.e. , much lower than the one achieved by SRIR. And even though AFM has much higher intrinsic resolution than optical microscopy, it cannot serve as a ground truth as AFM images can be blurred by tip geometry effects²⁴⁻²⁶. Furthermore, Raman spectroscopy and AFM measure fundamentally different material properties, so even if both techniques had indefinite resolution, identical images would not be expected (AFM, for instance, would not reveal any embedded nanoheterogeneity).

Resolution enhancement and regularisation

Resolution enhancement in SRIR is often achieved with the help of regularisation, which is simply adding a term of the form $\lambda\phi(x)$ to the optimisation criterion eq. (3a). Initially used as a heuristic to suppress noise artefacts in the restoration process, Bayesian analysis has managed to connect the regularisation function $\phi(\cdot)$ to prior knowledge about the super-resolved image¹. The regularisation parameter λ is usually chosen depending on the noise level in the observed low-resolution image. It has been recognised early that a large amount of prior information can be used to increase the resolution by a large amount³⁶. An excellent example from fluorescence imaging demonstrates the power of aptly chosen regularisation while simultaneously hinting at the difficulties involved in arriving at such an apt choice³⁷. The drawback of using regularisation is that prior information may not always be available to a sufficient degree, and even if it is, the choice of corresponding regularisation function $\phi(\cdot)$ and parameter λ may not be straightforward.

The results of this paper were obtained without regularisation. Noise suppression and high spatial frequency estimation were achieved by the positivity constraint eq. (3b) and primal-dual IPLS¹⁸ alone. This allows for SRIR of images for which no information about the super-resolved image is available a priori, apart from the generic assumption that the resulting pixel intensities should be positive. Simultaneously, if any additional prior knowledge about the super-resolved image is available, it can be straightforwardly implemented via a regularisation term in eq. (3a). This makes constrained optimisation via primal-dual IPLS a powerful and flexible tool for SRIR.

Below the sampling step size

The information received from a scanning stage microscope is band limited with the cut off frequency given by the inverse of the sampling step size. This means that by utilising the information received from the imaging process only it is impossible to resolve objects separated by less than a step size. By choosing appropriate constraints and regularisation, we are no longer restricted by the information theoretic limit as these provide a means to estimate Fourier coefficients above the cut off

frequency which, when aptly chosen, can push resolution enhancement even further.

In the case of the present experiment this can be observed in the line profile along section S2, fig. 6b. The profile of the 20nm pixel size super-resolved image shows one peak whereas two peaks are clearly distinguishable for 10nm pixel size. It could be argued that the observed gap of about 20nm between the two peaks constitutes the minimum resolvable distance achieved by SRIR, which would indeed be an extraordinary and flattering result. But there is no experimental evidence to support such a claim and dependent on whether such a gap is desired or not it is either a feature or an artefact of the method employed.

The primary aim of this work was only to go beyond the intrinsic diffraction limit of the confocal Raman microscope. The occurrence of sub-step size separations in the super-resolved image fig. 5b should only give an idea of the possibilities when the full power of SRIR is unleashed.

Conclusions

We have successfully applied SRIR to Raman data of PEDOT nanowires. A conservative estimate suggests an enhancement in spatial resolution of about a factor 3 relative to the confocal Raman microscope's intrinsic resolution. The minimum resolvable distances of 360nm and higher in the raw data have been reduced to 125nm and lower by application of SRIR.

The gain in resolution through SRIR constitutes true super-resolution in the microscopist's sense of resolution as it has been demonstrated on objects that are unresolved in the raw data. The high-resolution images obtained through the proposed SRIR method, primal-dual IPLS, show satisfactory agreement when compared to AFM data of the same scene.

The raw data was acquired using a conventional Raman microscope equipped with a motorised piezo stage. No near-field spectroscopic techniques such as NFRS or TERS were involved, thus adding no complexity to the experimental setup and avoiding any kind of electronic interaction with the sample material.

In addition we demonstrated and discussed the potential of primal-dual IPLS to resolve distances below the raw data sampling step size of 20nm. Faithful SRIR at such small scales would require thorough thermal

and mechanical stabilisation during the measurement process and will be the subject of a future investigation.

Further, the SRIR results of this paper were generated by processing data from only one spectral channel of the Raman microscope. Data from multiple channels would allow for the retrieval of chemical information with high spatial resolution and perhaps for further reduction of the minimum resolvable distance through SRIR with primal-dual IPLS. These would be desirable results as they would not require any additional measurements or experimental complications and will be addressed in future publications.

Declaration of conflicting interests

There are no conflicts to declare.

Funding

This work has received funding from the European Union's Horizon 2020 research and innovation programme under the Marie Skłodowska-Curie grant agreement No 642742.

References

1. S.C. Park, M.K. Park, M.G. Kang. "Super-resolution image reconstruction: A technical overview". *IEEE Sig. Process. Mag.* 2003. 20(3): 21–36.
2. R. Tsai, T. Huang. "Multiframe image restoration and registration". *Adv. Comput. Vis. Image Process.* 1984. 1: 317–339.
3. L. Duponchel, P. Milanfar, C. Ruckebusch et al. "Super-resolution and raman chemical imaging: From multiple low resolution images to a high resolution image". *Anal. Chim. Acta* 2008. 607(2): 168–175.
4. M. Tomita, H. Hashiguchi, T. Yamaguchi et al. "Super-resolution raman spectroscopy by digital image processing". *J. Spectrosc. (London, U. K.)* 2013. 2013: 459032.
5. M. Offroy, M. Moreau, S. Sobanska et al. "Pushing back the limits of raman imaging by coupling super-resolution and chemometrics for aerosols characterization". *Sci. Rep.* 2015. 5: 12303.
6. H. Cui, W. Zhao, Y. Wang et al. "Improving spatial resolution of confocal raman microscopy by super-resolution image restoration". *Opt. Express* 2016. 24(10): 10767–10776.
7. S. Webster, D.N. Batchelder, D.A. Smith. "Submicron resolution measurement of stress in silicon by near-field raman spectroscopy". *Appl. Phys. Lett.* 1998. 72(12): 1478–1480.
8. J. Grausem, B. Humbert, M. Spajer et al. "Near-field raman spectroscopy". *J. Raman Spectrosc.* 1999. 30(9): 833–840.

9. R.M. Stockle, Y.D. Suh, V. Deckert et al. "Nanoscale chemical analysis by tip-enhanced raman" spectroscopy". *Chem. Phys. Lett.* 2000. 318(1): 131–136.
10. L. Langeluddecke, P. Singh, V. Deckert." "Exploring the nanoscale: Fifteen years of tipenhanced raman spectroscopy". *Appl. Spectrosc.* 2015. 69(12): 1357–1371.
11. M.V. Afonso, J.M. Bioucas-Dias, M.A.T. Figueiredo. "An augmented lagrangian approach to the constrained optimization formulation of imaging inverse problems". *IEEE Trans. Image Process.* 2011. 20(3): 681–695.
12. P. Paatero. "Least squares formulation of robust non-negative factor analysis". *Chemom. Intell. Lab. Syst.* 1997. 37(1): 23–35.
13. D.D. Lee, H.S. Seung. "Learning the parts of objects by non-negative matrix factorization". *Nature* 1999. 401(6755): 788.
14. B.R. Hunt. "The application of constrained least squares estimation to image restoration by digital computer". *IEEE Trans. Comput.* 1973. 100(9): 805–812.
15. B.R. Frieden. "Restoring with maximum likelihood and maximum entropy". *J. Opt. Soc. Am.* 1972. 62(4): 511–518.
16. B.R. Frieden, J.J. Burke. "Restoring with maximum entropy, II: Superresolution of photographs of diffraction-blurred impulses". *J. Opt. Soc. Am.* 1972. 62(10): 1202–1210.
17. D.L. Donoho, I.M. Johnstone, J.C. Hoch et al. "Maximum entropy and the nearly black object". *J. Roy. Stat. Soc., Ser. B (Method.)* 1992. 54(1): 41–81.
18. E. Chouzenoux, M. Legendre, S. Moussaoui et al. "Fast constrained least squares spectral unmixing using primal-dual interior-point optimization". *IEEE J. Sel. Topics Appl. Earth Observ.* 2014. 7(1): 59–69.
19. J.L. Duvail, P. Retho, S. Garreau et al. "Transport and vibrational properties of poly (3, 4ethylenedioxythiophene) nanofibers". *Synth. Met.* 2002. 131(1): 123–128.
20. D. Funes-Hernando, M. Pelaez-Fernandez, D.J. Winterauer et al. "Coaxial nanowires as plasmon-mediated remote nanosensors". *Nanoscale* 2018. 10(14): 6437–6444.
21. G. Binnig, C.F. Quate, C. Gerber. "Atomic force microscope". *Phys. Rev. Lett.* 1986. 56(9): 930–933.
22. Q. Zhong, D. Inniss, K. Kjoller et al. "Fractured polymer/Silica fiber surface studied by tapping mode atomic force microscopy". *Surf. Sci. Lett.* 1993. 290(1): L688 – L692.
23. "Bruker OTESPA AFM tip description", 2018. URL <https://www.brukerafmprobes.com/p-3381-otespa.aspx>. Last accessed Jan 23 2019.
24. D.J. Keller, C. Chih-Chung. "Imaging steep, high structures by scanning force microscopy with electron beam deposited tips". *Surf. Sci.* 1992. 268(1): 333 – 339.
25. P. Markiewicz, M.C. Goh. "Atomic force microscopy probe tip visualization and improvement of images using a simple deconvolution procedure". *Langmuir* 1994. 10(1): 5–7.
26. C.V. Nguyen, Q. Ye, M. Meyyappan. "Carbon nanotube tips for scanning probe microscopy: fabrication and high aspect ratio nanometrology". *Meas. Sci. Technol.* 2005. 16(11): 2138.
27. Y. Goussard. "3D reconstruction in X-ray tomography: approach example for clinical data processing". In J. Giovannelli, J. Idier, editors. *Regularization and Bayesian Methods for Inverse Problems in Signal and Image Processing*. London, UK: ISTE Ltd., 2015. Pp. 1–30.

28. C.W. Helstrom. "Image restoration by the method of least squares". J. Opt. Soc. Am. 1967. 57(3): 297–303.
29. M. Elad, A. Feuer. "Restoration of a single superresolution image from several blurred, noisy, and undersampled measured images". IEEE Trans. Image Process. 1997. 6(12): 1646–1658.
30. S. Farsiu, M.D. Robinson, M. Elad et al. "Fast and robust multiframe super resolution". IEEE Trans. Image Process. 2004. 13(10): 1327–1344.
31. L.W. Davis. "Theory of electromagnetic beams". Phys. Rev. A 1979. 19: 1177–1179.
32. M. Lax, W.H. Louisell, W.B. McKnight. "From maxwell to paraxial wave optics". Phys. Rev. A 1975. 11(4): 1365–1370.
33. H. Kogelnik, T. Li. "Laser beams and resonators". Appl. Opt. 1966. 5(10): 1550–1567.
34. G.D. Boyd, J.P. Gordon. "Confocal multimode resonator for millimeter through optical wavelength masers". Bell Syst. Tech. J. 1961. 40(2): 489–508.
35. R.H. Webb. "Confocal optical microscopy". Rep. Prog. Phys. 1996. 59(3): 427–471.
36. G.T. di Francia. "Resolving power and information". J. Opt. Soc. Am. 1955. 45(7): 497–501.
37. S. Hugelier, J.J. De Rooi, R. Bernex et al. "Sparse deconvolution of high-density superresolution images". Sci. Rep. 2016. 6: 21413.
38. L. Rayleigh. "XV. On the theory of optical images, with special reference to the microscope". Philos. Mag. (1798-1977) 1896. 42(255): 167–195.
39. B. Richards, E. Wolf. "Electromagnetic diffraction in optical systems, II. structure of the image field in an aplanatic system". Proc. R. Soc. London, Ser. A 1959. 253(1274): 358–379.
40. G.B. Airy. "On the diffraction of an object-glass with circular aperture". Trans. Cambridge Philos. Soc. 1835. 5: 283–291.
41. E.H. Stelzer. "Contrast, resolution, pixelation, dynamic range and signal-to-noise ratio: fundamental limits to resolution in fluorescence light microscopy". J. Microsc. (Oxford, U. K.) 1998. 189(1): 15–24.

Supplemental material

The point-spread function and resolution

The point-spread function (PSF) of an optical microscope is the image observed from a single point-like scatterer. Its form and width determines the instrument's resolution. The minimum resolvable distance Δr in a confocal microscope is given by the diffraction or Rayleigh limit^{35,38}

$$\Delta r = 0.44 \frac{\lambda}{n NA}, \quad (8)$$

where λ is the wavelength of the observed light, n the refractive index of the medium and NA the numerical aperture of the objective lens. For a system with $\lambda = 532nm$, $n = 1$ and $NA = 0.85$ eq. (8) yields $\Delta r = 275nm$.

This constitutes the theoretically optimal case for which the PSF can be found in^{35,39}. The shape of the PSF is tightly connected to the resolution of an optical instrument. Airy described the diffraction pattern of a self-luminous point-source (star) under an object-glass with circular aperture⁴⁰, which is just the PSF of his instrument. Rayleigh later proposed to define the minimum resolvable distance Δr as the lateral distance from the optical axis for which the Airy diffraction pattern attains its first minimum³⁸. The intensity dip between two self-luminous point-like objects of equal intensity (wide-field illumination) separated by Δr is about 26.4% the maximum intensity^{35,41}. Rayleigh's original definition of Δr is specific to the Airy diffraction pattern, but it has been extended to instruments that do not exhibit an Airy diffraction pattern as the lateral separation of two equiluminous point sources that yields a 26.4% dip between the two maximum intensities observed^{35,41}. Modern descriptions of resolution, however, tend away from absolute values for Δr and rather state it for a given value of contrast^{35,41}.

For a Gaussian PSF like in eq. (4) Rayleigh's Δr along each axis can be approximated by

$$\Delta r_{\{x,y\}} \approx 2.80\sigma_{\{x,y\}}. \quad (9)$$

Another commonly used experimental measure is the full width at half maximum (FWHM) of the PSF. The FWHM for eq. (4) is given by

$$\text{Two equiluminous sources} \quad FWHM_{\{x,y\}} = 2p2\log(2)\sigma_{\{x,y\}} \quad (10a)$$

$$\text{separated by FWHM will} \quad \approx 2.35\sigma_{\{x,y\}}. \quad (10b)$$

show a dip of 7.3% of the maximum intensity when observed through a microscope with Gaussian PSF. A separation of less than $2\sigma_{\{x,y\}}$ for the PSF eq. (4) produces no dip between two objects, regardless of their relative luminosity, and is thus unresolvable.

Super-resolution of simulated test images

The primal-dual algorithm used in this paper¹⁸ for solving the interior-point least squares (IPLS) problem eq. (3) can be tested on computer generated images. From a given ground truth an observed image can be calculated by application of the observation model eq. (1). The observed image can then be super-resolved and compared to the given ground truth. Two simple cases are considered:

i) two identical parallelograms aligned parallel to each other with shorter edges of $80nm$, longer edges of $870nm$, and minimum separation of $110nm$, fig. 7a; ii) one parallelogram with shorter edge of $270nm$ and longer edge of $870nm$, fig. 8a. Case (ii) is the same as case (i) but with the gap between the two parallelograms filled. Both generated ground truths have a pixel size of $10nm \times 10nm$.

Each ground truth was convolved with a Gaussian PSF given in eq. (4) with $\sigma_x = 200nm$ ($FWHM_x = 471nm$) and $\sigma_y = 150nm$ ($FWHM_y = 353nm$), downsampled to images of pixel size $20nm \times 20nm$, and added to i.i.d. Gaussian noise with a signal-to-noise ratio (SNR) of $30dB$ to yield the respective observed images, figs. 7b and 8b. Super-resolution image restoration (SRIR) with IPLS was then performed with two different forward operators on each of the simulated observations. The first choice of forward operator was convolution with the PSF used in generating the simulated observations, resulting in high-resolution images of pixel size $20nm \times 20nm$, figs. 7c and 8c. The second choice of forward operator was the full forward operator used for generating the simulated observations, i.e. convolution with the PSF and downsampling by a factor of 2 along each image axis, resulting in high-resolution images of pixel size $10nm \times 10nm$, figs. 7d and 8d.

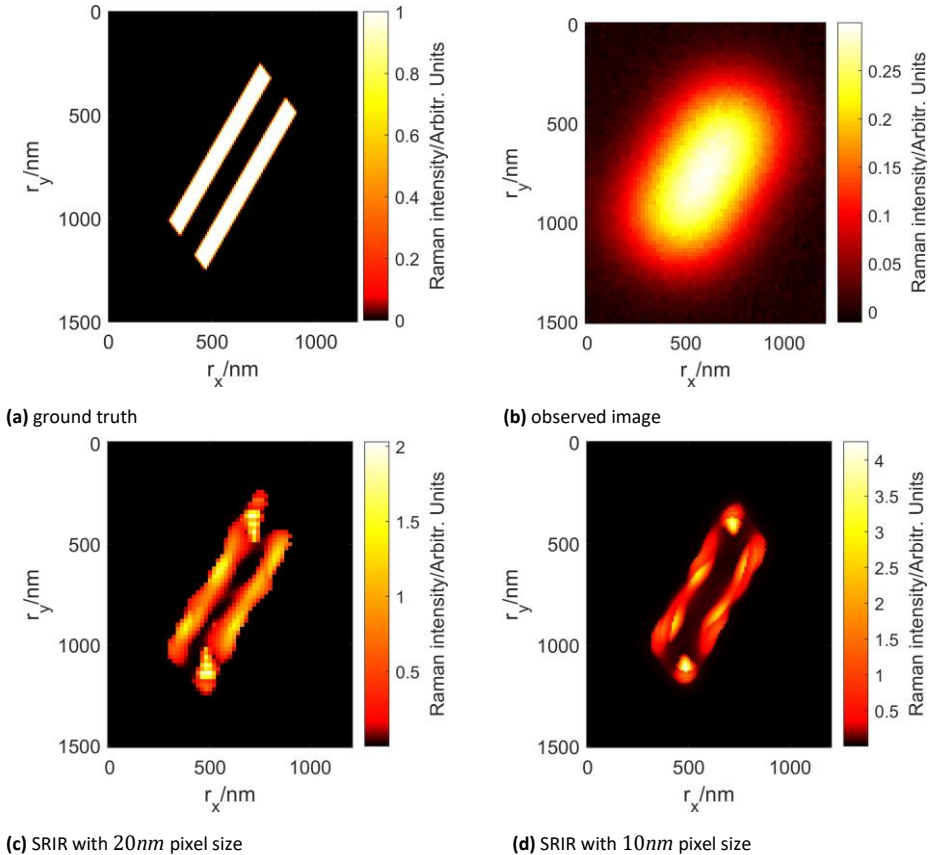


Figure 7. Demonstration of IPLS on a numerical test image: (a) Simulated ground truth with pixel size of $10nm \times 10nm$; (b) observed image after convolution with the PSF of eq. (4) with $\sigma_x = 200nm$ and $\sigma_y = 150nm$, downsampling (pixel size $20nm \times 20nm$), and the addition of Gaussian white noise with $SNR = 30dB$; (c) result of IPLS without up-/downsampling (pixel size $20nm \times 20nm$); (d) result of IPLS with up-/downsampling (pixel size $10nm \times 10nm$)

The results of IPLS, figs. 7c and 7d and figs. 8c and 8d, are by no means perfect restorations, as can be seen by comparison with the respective ground truths fig. 7a and fig. 8a. Because the size of the objects in the ground truth images is smaller than the width of the PSF along at least one dimension a perfect restoration would not be expected. However, the resulting super-resolved images figs. 7c and 7d and figs. 8c and 8d are qualitatively very different, in resemblance of the respective ground truth, despite the large similarity between the observed images fig. 7b and fig. 8b.

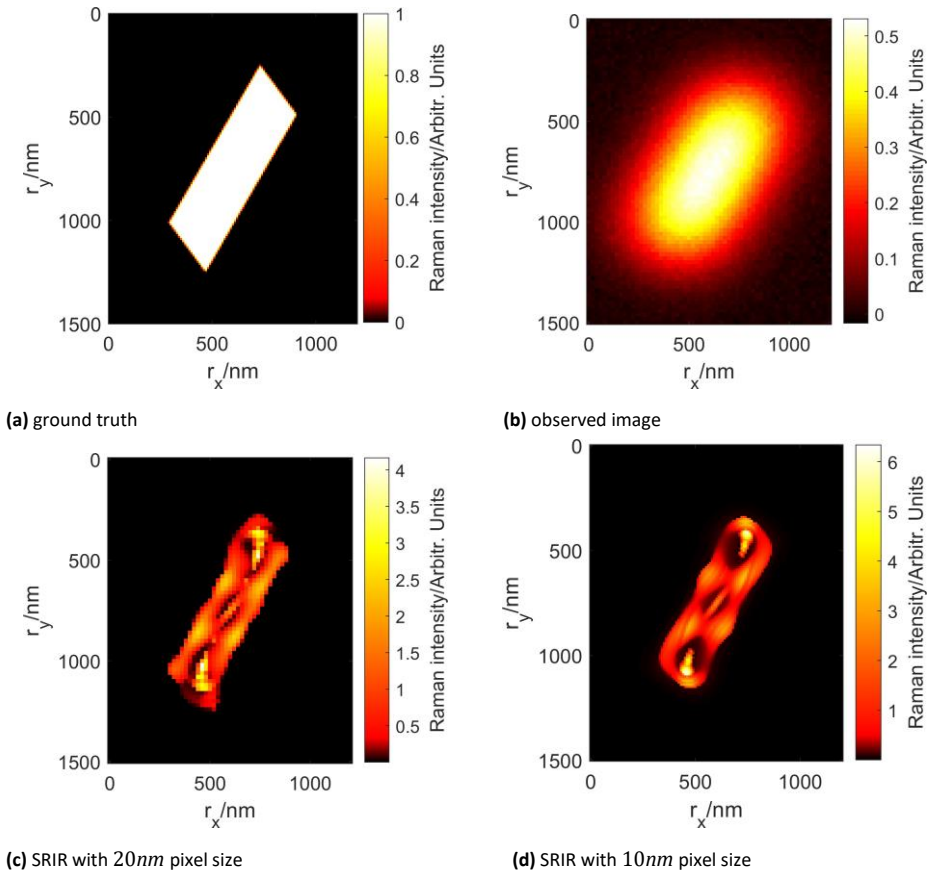


Figure 8. Demonstration of IPLS on a numerical test image: (a) Simulated ground truth with pixel size of $10\text{nm} \times 10\text{nm}$; (b) observed image after convolution with the PSF of eq. (4) with $\sigma_x = 200\text{nm}$ and $\sigma_y = 150\text{nm}$, downsampling (pixel size $20\text{nm} \times 20\text{nm}$), and the addition of Gaussian white noise with $\text{SNR} = 30\text{dB}$; (c) result of IPLS without up-/downsampling (pixel size $20\text{nm} \times 20\text{nm}$); (d) result of IPLS with up-/downsampling (pixel size $10\text{nm} \times 10\text{nm}$)